Spatial–Temporal Analyses of Surface Coal Mining Dominated Land Degradation in Holingol, Inner Mongolia

Tana Qian, Hasi Bagan, *Member*, *IEEE*, Tsuguki Kinoshita, and Yoshiki Yamagata

***Abstract*—Surface coal mining and urbanization, as well as crop-based agriculture, have resulted in accelerated degradation and desertification of grasslands in the Holingol region, Inner Mongolia Autonomous Region, over the last three decades. The purpose of this study was to investigate the spatial–temporal changes of land cover due to the surface coal-mining activities in the Holingol region from 1978 to 2011. In this study, we used the subspace method to apply land-cover classification schemes to Landsat archival images from 1978, 1988, 1999, and 2011. We then used the grid square method to investigate spatial–temporal land-cover changes during the period of 1978–2011. The results show that both surface coal mining and urban areas have increased dramatically. This expansion was accompanied by considerable loss of grassland and wetland. Grid-cell-based spatial–temporal analysis showed that urban/bare expansion had a strong negative correlation with grassland change (-0.67), coal-mining area expansion had a negative correlation with grassland change (-0.29), and coal-mining area expansion was positively correlated with urban/bare expansion (0.21). Furthermore, the correlation coefficients of land-cover categories for three time intervals between 1978 and 2011 (1978–1988, 1988–1999, and 1999–2011) showed that there was almost no correlation between grassland and coal-mining area in 1978–1988 and 1988–1999, but the correlation coefficient became negative (-0.21) in 1999–2011.**

***Index Terms*—Grassland degradation, grid cells, land cover, surface coal mining, urban expansion.**

I. Introduction

THE Holingol region is located in the northern part of the Horqin Sandy Land in the Inner Mongolia Autonomous Region of China. The Holingol study area includes the city of Huolinguole, as well as parts of East Ujimqin, West Ujimqin, Ar Horqin, Jarud, Horqin Right Middle, and Horqin Right Front Banners. Previous studies indicate that population increase, excessive land development, overgrazing, and collection of fuel wood have been the main driving forces in Horqin's desertification process [1]–[3]. In recent decades, China's demand for coal for power generation has put the coal-rich Holingol region under strong pressure, and a surface coal-mining boom has emerged. The dramatic increase in coal-mine exploitation has lately generated major concern regarding the fragile environment of this region. In addition, a recent study estimates that coal pollution in North China is shortening life expectancy by 5.5 years [4].

The first surface coal mine in this region was the Holingol open pit coal mine, which began in 1979 with a coal production capacity of 300 000 tons per year. By 2004, however, the coal production capacity had dramatically expanded to 12 500 000 tons per year. Furthermore, new mining operations in this region at the Baiyinhua and Hesigewula open pit coal mines were introduced in 2005 and 2007.

Rich coal reserves coupled with low-cost mining attracted unregulated exploitation that has brought dramatic land-cover changes to this area. Most of the coal production in this area is achieved by surface mining in which large volumes of waste materials are excavated and removed from one place to another causing a continuous change of natural land cover and topography over time [5].

Furthermore, coal mining, coal-based power generation, and petrochemical processing are extremely water intensive. To meet the water demands of coal-based industries, local rivers, and their tributaries have been dammed and many wells have been dug. A recent analysis found that the Wulagai wetland, which is located in this region, has gone dry due to the overuse of groundwater and surface water [6]. However, to our knowledge, no detailed quantitative analysis concerning the land degradation rates under the surface coal-mining activities in the Holingol region has been published.

The coal-driven boom not only has exacerbated existing environmental problems by exploiting water resources, altering landscapes, and discharging wastewater onto rivers and grasslands, but also has led to new concerns particularly related to urbanization issues. For example, the population of Huolinguole has increased by about a factor of three, from 29 897 in 1985 to 82 430, in 2010 [7]. Meanwhile, the population of migrant agricultural workers has also increased rapidly; as a result, a large area of grassland has been turned into farmland [8]. The nomadic grazing tradition has also been weakened, making room for more intensive land management [9].

As natural land cover is converted into human-dominated cover types, the fragile environment has experienced a remarkable change [10]. Assessing and monitoring of surface coal

Manuscript received February 25, 2013; revised October 16, 2013; accepted January 06, 2014. Date of publication February 06, 2014; date of current version June 13, 2014. This work was supported by the Environment Research and Technology Development Fund (S-10) of the Ministry of the Environment, Japan.

T. Qian is with the Center for Global Environmental Research, National Institute for Environmental Studies, Tsukuba, Ibaraki 305-8506, Japan, and also with the College of Agriculture, Ibaraki University, Amimachi, Ibaraki 300-0393, Japan (e-mail: tana.qian@nies.go.jp).

H. Bagan and Y. Yamagata are with the Center for Global Environmental Research, National Institute for Environmental Studies, Tsukuba, Ibaraki 305-8506, Japan (e-mail: hasi.bagan@nies.go.jp).

T. Kinoshita is with the College of Agriculture, Ibaraki University, Amimachi, Ibaraki 300-0393, Japan (e-mail: kino@mx.ibaraki.ac.jp).

Color versions of one or more of the figures in this paper are available online at http://ieeexplore.ieee.org.

Digital Object Identifier 10.1109/JSTARS.2014.2301152

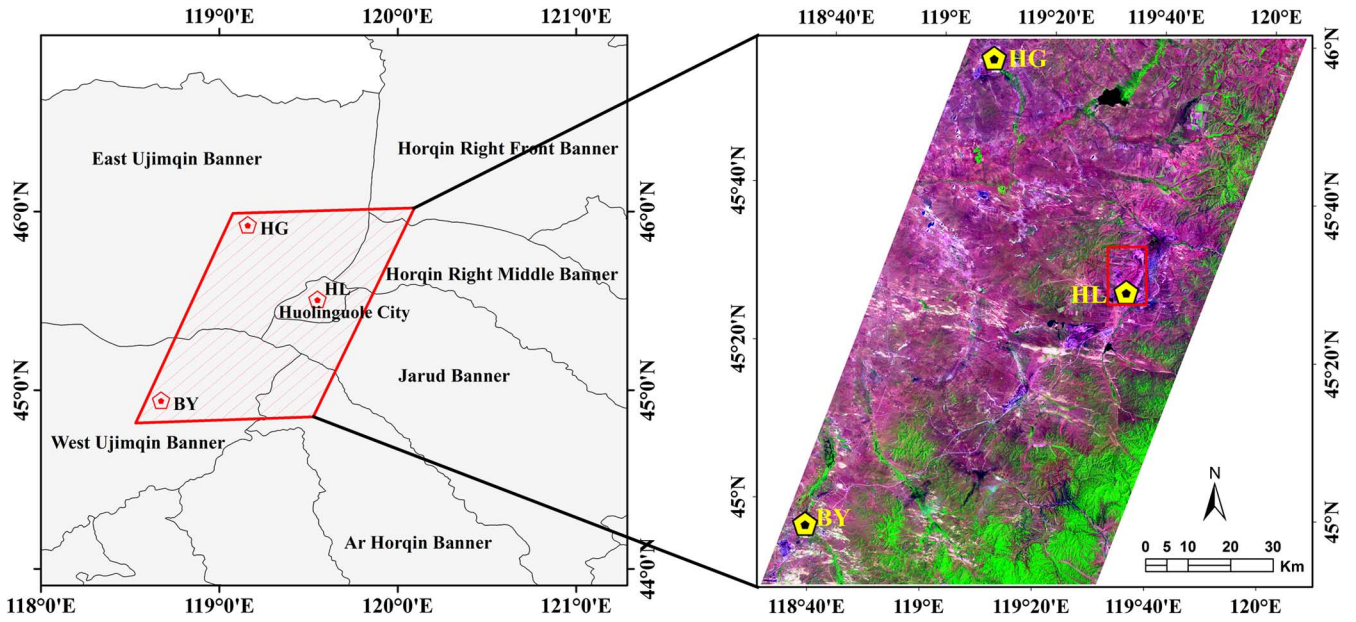

Fig. 1. Location of the study area (red quadrangle on the left side). The black lines outline the boundaries of the city and banners. The three red marks within the red quadrangle indicate the three main coal fields in Holingol: HL, HG, and BY indicate the Holingol, Hesigewula, and Baiyinhua coal fields, respectively. The right side shows the 2011 Landsat TM image (RGB = bands $5, 4, 3$) of the study area. The red rectangle indicates the area of the images shown in Fig. 5.

mining is crucial for obtaining knowledge of the kind, type, and degree of land-use/land-cover changes and regional ecosystems degradation caused by surface coal mining [11]. Moreover, it yields the locations and rate of human pressure on natural resources and the type of land cover on which this pressure may reach critical levels [12].

Remotely sensed data collected over a span of years can be used to identify and characterize both natural and anthropogenic changes over large areas of land [13], [14]. Landsat satellite images are ideal for land monitoring as the images have been recorded over nearly four decades, providing a unique resource for temporal analysis of land cover [15]. Various approaches have been developed for land-cover classification [16]. A main source of classification error is the indivisibility of classes. To reduce classification errors, it is desirable to find a method that transforms the input high-dimensional data into low-dimensional feature space to reduce overlap between classes and to preserve the main properties of the original data [17]. The subspace method is one such transformation method [18]. Recently, developed subspace methods have been used to solve remote sensing image classification problems and have shown potential for efficient classification of remote sensing data [19].

For detailed analysis of the relationships among changes in landscape patterns, it is necessary to obtain spatial and temporal information about areas that are smaller than municipalities and uniform in size. Using a municipality's boundary as the mapping unit in an analysis has shortcomings: the size and boundaries of administrative units of local municipalities may change over time [20], they may not be uniform enough for statistical and numerical processing, and the spatial resolution may be too coarse for identifying land-use/land-cover changes.

Recently, spatial–temporal analyses of land-cover changes using $1\ \mathrm{km}^2$ grid cells have demonstrated that grid cells provide a new way to obtain spatial and temporal information about areas that are smaller than the municipal scale and uniform in size [21] and to further develop the change dynamics analysis in order to better characterize the phenomena using limited available data.

The purpose of this study was to investigate the spatial–temporal changes of land cover due to the open-cast surface coal-mining activities in the Holingol region from 1978 to 2011, by integrating remote sensing images, GIS, and detailed field work. To do this, we applied the subspace classification method to accurately classify land cover from Landsat images recorded in 1978, 1988, 1999, and 2011. These land-cover maps were then combined with $1\ \mathrm{km}^2$ grid cells to analyze the spatial–temporal land-cover changes and investigate their statistical properties. This allowed us to determine the impact of surface mining activities on the environment and land use over a time period of more than three decades.

II. Materials

A. Study Area

The study area is the Holingol region, located in the northern part of the Horqin Sandy Land of the Inner Mongolia Autonomous Region, China, and centered at $45°24'\mathrm{N}, 119°15'\mathrm{E}$ (Fig. 1). The climate is characterized by extremes, with high temperatures in the summer and extremely low temperatures in the winter, as well as low precipitation. This territory includes a variety of ecosystems such as the forest, steppe, wetland, mountain, and desert.

Huolinguole, which is a new coal-resource-based industrial city, is located in the centre of Holingol region. The climate of Huolinguole can be regarded as representative of this region. The monthly mean temperature ranged from $-19.4\,°\mathrm{C}$ in January to $19.5\,°\mathrm{C}$ in July, during the period of 1973–2006. The annual mean precipitation ranged from 193.1 to 654.8 mm. In contrast, the annual mean potential evaporation of 1544.2 mm is far higher than the annual precipitation.

TABLE I
PATH/ROW AND ACQUISITION DATES FOR THE LANDSAT TIME-SERIES SCENES USED IN THIS STUDY

Sensors	Date acquired	Path/row	Location	Spatial resolution (m)
Landsat-3 MSS	1978-06-21	132/28	Main	60
	1978-06-21	132/29	Main	
	1978-08-31	131/28	East	
Landsat-5 TM	1988-08-04	122/28	Main	30
	1989-06-20	122/29	Southwest	
Landsat-7 ETM+	1999-08-11	122/28	Main	30
	1999-08-11	122/29	Main	
	2002-08-26	123/29	Southwest	
Landsat-5 TM	2011-06-17	122/28	East	30
	2011-06-17	122/29	East	
	2011-08-11	123/28	Main	
	2011-08-11	123/29	Main	

B. Dataset Description

We acquired Landsat MSS, TM, and ETM+ images to interpret land-use/land-cover changes for the study area from four separate dates (nominally 1978, 1988, 1999, and 2011). Landsat scenes are processed for standard terrain corrections by the U.S. Geological Survey (USGS). Table I provides the image dataset description. In consideration of the weather conditions, only images from June to August, the green vegetation season, and with low cloud cover were used to maximize the vegetation information content for each monitoring date. All analyses were based on the optical and thermal infrared bands of the MSS, TM, and ETM+ data, while excluding panchromatic bands. The spatial resolution of the MSS bands was approximately 79 m, but these data were resampled to 60 m by using the cubic convolution method employed by the USGS.

Precise geometric registration to a common map reference and co-registration among individual images are crucial for ensuring the reliable detection of temporal changes of land cover. The Landsat scenes were rectified through an image-to-image operation and resampled using a nearest neighbor algorithm to preserve the reflectance of the original pixels. All Landsat images were geometrically rectified to a common map reference system (UTM map projection Zone 51 North, WGS-84 geodetic datum) using a different number (around 25–36) of ground control points (GCPs) for each image.

The June 1978 MSS images contained cloud cover and associated shadows on the right-hand side of the study area, so we used a mosaic of June and August 1978 MSS images to generate a "cloud-free" image mosaic. Here, we isolated the clouds and their associated shadow portions of the June image by visual image interpretation, then substituted the selected portions with clear pixels from the August 1978 MSS scene (131/28) of the same area. The August 1988 TM data did not cover a small area in the south-western region of the study area, so we used a mosaic of August 1988 TM and June 1989 data to attain full area coverage. The data from August (122/28) was used as the primary base image because it accounted for about 90% of the total study area, and the June 1989 (122/29) was used for patching the south-western part (this mosaic is hereafter referred to as the 1988 TM data). The August 1999 ETM+ data had the same incomplete image problem, so we used August 1999 ETM+ data (122/28 and 122/29) for primary base image data, and the August 2002 ETM+ data (123/29) was used for patching the south-western region (this mosaic is hereafter referred to as the 1999 ETM+ data). The August 2011 TM data lacked the right-hand edge of the study area, so we used the August 2011 TM data (123/28 and 123/29) for primary base image data, and the June 2011 TM data (122/28 and 122/29) was used for patching the right-hand edge of the study area.

For minimizing the contrast between the two images in the final mosaic, a histogram matching method was applied to adjust the distribution of brightness values in the slave image (patch scene) to match the master scene (base scene). In addition, to reduce spectral variation in the mosaic image and to improve classification results, we used images collected during the summer growing season in order to reduce spectral signature variation caused by seasonal differences in plant phenology [22]. Moreover, the proportions of patch imagery to base imagery in the mosaic were small.

In addition to Landsat data, ancillary GIS datasets and other ancillary satellite data were used as reference data to assist in our field investigation in the determination of typical land-cover classes and in selecting ground reference sites for each Landsat recording date. The GIS datasets included data from the National Land Cover Database (NLCD) of China from the years 1995 and 2000 at a spatial scale of 1:100 000 [23] and from Resources and Environment Database of China digital maps at a scale of 1:4 000 000 [24], including a vegetation map (published in 1979), soil map (1978), desert map (1988), road map (1988), and river map (1989). Remote sensing data included ALOS PRISM images (panchromatic, 2.5-m spatial resolution) and AVNIR-2 (10-m spatial resolution, three visible bands, and one near-infrared band) images acquired on October 7, 2007; four WorldView-2 images with 0.46-m panchromatic and 1.84-m multispectral resolutions acquired in May to August 2012; a GeoEye-1 satellite image with 0.41-m panchromatic and 1.65-m multispectral resolutions acquired on August 3, 2009 (provided by the GeoEye Foundation); four Landsat MSS scenes; nine Landsat TM scenes; and six Landsat ETM+ scenes. Other ancillary data such as Shuttle Radar Topography Mission (SRTM) elevation data were used to provide information about the elevation of the area and to help locate ground reference sites.

C. Collection of Ground Truth Data

To obtain the ground truth data, we have conducted extensive field work at a number of locations across the study area in the period between 2000 and 2007 [3] and in 2012. During the field

surveys, photos were taken for ground reference data with GPS facilities and land-cover types were recorded in the land-use/land-cover recording sheet. In addition, local herders and farmers were visited to verify current and past land-cover patterns and discuss the drivers of land-cover changes.

Based on the field investigation results, GIS datasets, visual interpretation of the remote sensing data, and with consideration of the Landsat scene acquisition dates, we designated 10–12 land-cover types in this experiment (Table II).

According to our fieldwork results, in 1978, the study area was dominated by those practicing a traditional nomadic lifestyle, and there were only a few concrete buildings and unpaved roads. The Holingol open pit coal mine was still in its earlier preparation plan in 1978. Therefore, we did not add the urban and coal land-cover types in the 1978 MSS.

Since the 1990s, the migration of people has rapidly increased the human population of the grassland areas in the Holingol region. Consequently, the land area developed for agricultural use has expanded. The rapid agricultural expansion caused land degradation and alkali soils to become a serious problem in this region. So, we added the alkali soils land-cover class to the 1999 ETM+ and 2011 TM images.

Ground reference data sites were selected for each mapping class and for each mosaic Landsat recording date to accurately portray the spectral complexity and variability within each class. All initial digitized ground reference sites were compared with the corresponding Landsat imagery acquired in 1978, 1988, 1999, and 2011 to provide the correct interpretation for the time of the image date. In addition, as described above, other ancillary images and ancillary GIS datasets were used to support image interpretation and to provide as much information as possible to help locate the ground reference sites.

When a sample site contained multiple classes or was poorly delineated, a new homogeneous sample polygon (or line) was delineated within the original site. It is important to note that each sample site contains at least nine pixels [25]. A subset of the image-interpreted sites was also field visited and additional sites were collected. The training and test samples were selected from ground reference sites by manual digitization to ensure that they were spatially separated and to reduce the potential for correlation between the study and test data [25]. Fig. 2 shows some typical landscapes in the study area.

III. Methods

A. Subspace Classification

The subspace method was applied to each of the four dataset groups (Table I). Subspace methods [18], widely used for pattern recognition and computer vision, have been applied to remote sensing data classification [26]. The subspace method is a supervised classification method. In this method, high-dimensional input data are projected onto a low-dimensional feature space, and the different classes are then represented in their own low-dimensional subspace. The following is a description of the subspace method procedure.

In the preprocessing step, the training samples are normalized as follows. Let d be the input data dimension, which is equal to the number of bands. For a given pixel $\mathbf{x} = (x_1, x_2, \ldots, x_d)^T$, the normalized pixel is computed as

$$\mathbf{x} = (x_1/L, x_2/L, \ldots, x_d/L)^T \tag{1}$$

where $L = \sqrt{x_1^2 + x_2^2 + \cdots + x_d^2}$ is the pixel length. To be concise, we also use $\mathbf{x}$ to denote a normalized pixel.

Let $\varphi_{k,i}\,(1 \le i \le r, 1 \le k \le K)$ be the basis vectors of the subspace of class C^k, which are computed from class training samples by eigenvalue and eigenvector solving algorithms; where r denotes the subspace dimension and K denotes the number of classes. The projection length of pixel $\mathbf{x}$ in a subspace of class C^k is given by

$$P_k = \sum_{i=1}^{r} (\mathbf{x}, \phi_{k,i})^2. \tag{2}$$

After computing the projection length between pixel $\mathbf{x}$ and each subspace, pixel $\mathbf{x}$ is then labeled by the class that has the largest projection length.

Misclassifications may occur when class subspaces overlap. To separate them, the subspaces are slowly rotated to reduce the overlap between them. The main steps are described as follows.

At iteration k, the conditional correlation matrix is computed by

$$P_k^{(i,j)} = \sum_{\mathbf{x}} \left\{ \mathbf{x}\mathbf{x}^T \middle| \mathbf{x} \in C^i, \mathbf{x} \mapsto C^j \right\} \tag{3}$$

where the symbol $\mapsto$ denotes that the training sample $\mathbf{x}$ belonging to class C^i has been misclassified into class C^j.

Once the conditional correlation matrix is generated, the correlation matrix for class C^i is updated as follows:

$$P_k^{(i)} = P_{k-1}^{(i)} + \alpha \sum_{j=1, j\neq i}^{K} P_k^{(i,j)} - \beta \sum_{j=1, j\neq i}^{K} P_k^{(j,i)}, \tag{4}$$

where α and β are learning parameters, both usually with small positive constant values. Then, the eigenvalues and eigenvectors of $P_k^{(i)}$ are calculated to generate a new subspace of class C^i. The iterations end when either all the training data are fully recognized or the maximum number of iterations has been reached. Usually, by choosing the same subspace dimension and setting the two learning parameters equal to each other, higher recognition accuracy can be achieved [21].

B. Grid Cell Process

We made $1\ \mathrm{km}^2$ grid square cells, each given a unique ID number in the study area by using ArcGIS10 software. The advantage of grid square cells is that it can avoid the potential problem of changing boundaries of administrative units during the time interval of interest. Here, we chose $1\ \mathrm{km}^2$ as the cell size, because a $1\ \mathrm{km}^2$ cell covered more than 1000 TM pixels or 270 MSS pixels, and thus can facilitate our statistical analysis purposes. Grid squares with unique cell IDs enable us to link among land-cover maps for spatial–temporal land-cover change analysis. To do this, it is necessary to represent the land-cover maps in grid square cells.

TABLE II
DESCRIPTION OF THE LAND-COVER CLASSIFICATION SYSTEM AND THE NUMBER OF TRAINING AND TEST SAMPLES FOR IMAGES ACQUIRED IN (A) 1978, (B) 1988, (C) 1999, AND (D) 2011

Land-cover class	Class description	Training	Testing
(a) Land-cover classes and the number of training and test samples for image acquired in 1978			
1. Water	Permanent water bodies, rivers, lakes, and ponds	273	209
2. Forest	Forest with a mosaic of broadleaf trees, conifer and shrubbery, artificial forest, and woodlands along rivers	516	491
3. Grassland	Dominated by grasses and shrubs. Generally, vegetation accounts for 20% to 50% of total land cover	398	369
4. Sparse	Dominated by grasses, occasional trees and shrubs. Generally, vegetation accounts for 5% to 20% of total land cover	195	203
5. Barren	Bare soils, dry riverbed, unpaved roads, and villages	353	195
6. Sand dune	Covered in or consisting mostly of sand	272	238
7. Wetland	Mixture of water and herbaceous	350	302
8. Cropland	Crop	186	165
9. Dense	Areas dominated by grasses and shrubs with greater than 50% vegetation cover, mainly distributed in humid regions	285	217
Total		2828	2389
(b) Land-cover classes and the number of training and test samples for image acquired in 1988			
1. Water	Permanent water bodies, rivers, lakes, and ponds	921	686
2. Forest	Forest with a mosaic of broadleaf trees, conifer and shrubbery, artificial forest, and woodlands along rivers	1709	1343
3. Grassland	Dominated by grasses and shrubs. Generally, vegetation accounts for 20% to 50% of total land cover	1617	1481
4. Sparse	Dominated by grasses, occasional trees and shrubs. Generally, vegetation accounts for 5% to 20% of total land cover	901	882
5. Urban	All residential and industrial areas, mining buildings, and transport network	312	228
6. Sand dune	Covered in or consisting mostly of sand	925	727
7. Wetland	Mixture of water and herbaceous	765	676
8. Cropland	Crop	513	516
9. Barren	Bare soils, dry riverbed, unpaved roads, and waste dumps in open-cast mining	673	495
10. Coal	Coal stockpiles	310	91
11. Dense	Areas dominated by grasses and shrubs with greater than 50% vegetation cover, mainly distributed in humid regions	819	643
Total		9465	7768
(c) Land-cover classes and the number of training and test samples for image acquired in 1999			
1. Water	Permanent water bodies, rivers, lakes, and ponds	1213	1052
2. Forest	Forest with a mosaic of broadleaf trees, conifer and shrubbery, artificial forest, and woodlands along rivers	872	700
3. Grassland	Dominated by grasses and shrubs. Generally, vegetation accounts for 20% to 50% of total land cover	1553	1479
4. Sparse	Dominated by grasses, occasional trees and shrubs. Generally, vegetation accounts for 5% to 20% of total land cover	390	345
5. Urban	All residential and industrial areas, mining buildings, and transport network	363	284
6. Sand dune	Covered in or consisting mostly of sand	724	443
7. Wetland	Mixture of water and herbaceous	561	489
8. Cropland	Crop	666	601
9. Barren	Bare soils, dry riverbed, unpaved roads and waste dumps in open-cast mining	1271	974
10. Coal	Coal stockpiles	436	336
11. Dense	Areas dominated by grasses and shrubs with greater than 50% vegetation cover, mainly distributed in humid regions	707	638
12. Alkali	Alkali soils, in which less than 5% of land is covered by vegetation	711	511
Total		9467	7852
(d) Land-cover classes and the number of training and test samples for image acquired in 2011			
1. Water	Permanent water bodies, rivers, lakes, and ponds	1078	739
2. Forest	Forest with a mosaic of broadleaf trees, conifer and shrubbery, artificial forest, and woodlands along rivers	1567	1375
3. Grassland	Dominated by grasses and shrubs. Generally, vegetation accounts for 20% to 50% of total land cover	1609	1330
4. Sparse	Dominated by grasses, occasional trees and shrubs. Generally, vegetation accounts for 5% to 20% of total land cover	637	628
5. Urban	All residential and industrial areas, mining buildings, and transport network	712	654
6. Sand dune	Covered in or consisting mostly of sand	1065	1022
7. Wetland	Mixture of water and herbaceous	811	783
8. Cropland	Crop	835	621
9. Barren	Bare soils, dry riverbed, unpaved roads and waste dumps in open-cast mining	1101	1037
10. Coal	Coal stockpiles	1026	734
11. Dense	Areas dominated by grasses and shrubs with greater than 50% vegetation cover, mainly distributed in humid regions	946	720
12. Alkali	Alkali soils, in which less than 5% of land is covered by vegetation	800	735
Total		12 187	10 378

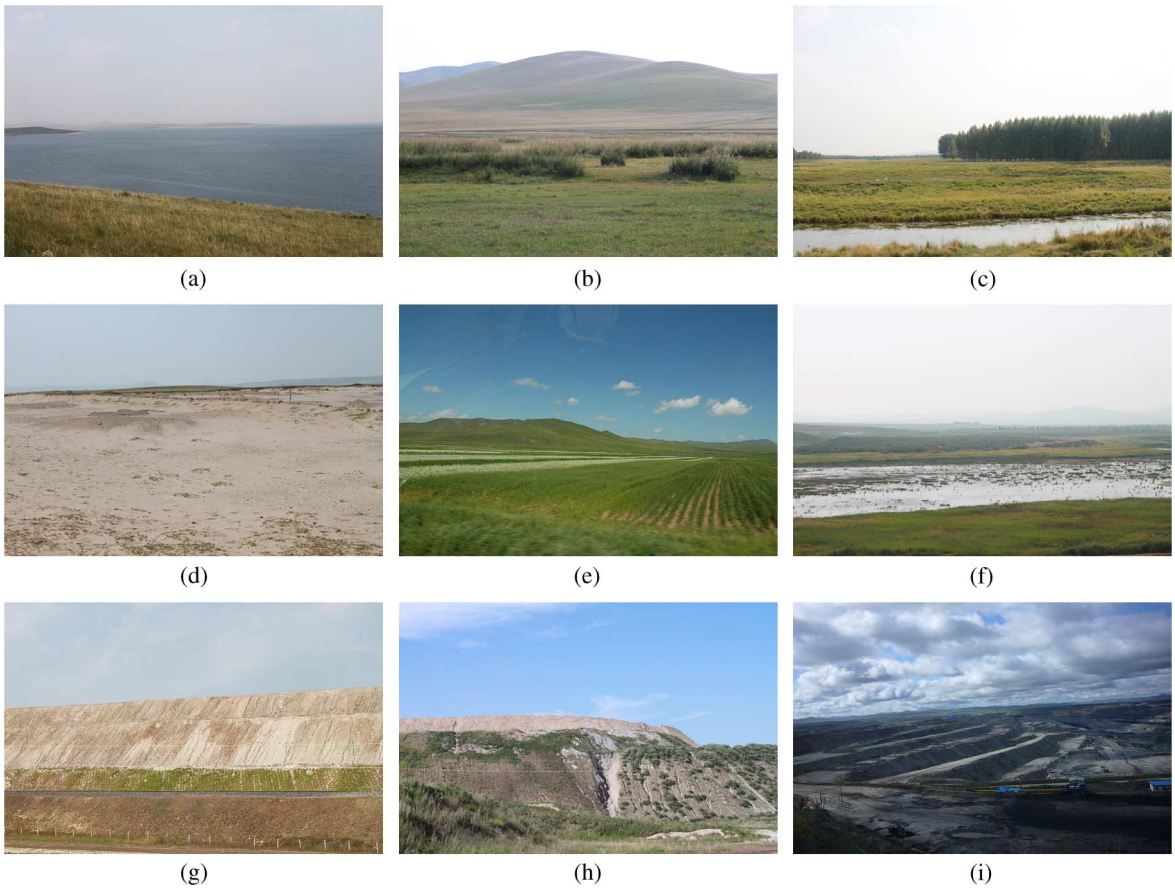

Fig. 2. Various landscapes in the study area: (a) water, (b) grassland, (c) woodland, (d) sandy land, (e) cropland, (f) wetland, (g) overburden dump at a coal-mining site, (h) overburden dump covered with vegetation, and (i) coal-mining site.

First, we merged similar categories of land cover into six main land-cover classes for analysis convenience, namely, water, forest, grassland, urban/bare, cropland, and coal. Here, we aggregated the grassland, sparse, dense grass, and wetland into a common "grassland" class and merged urban, bare soil, sand dune, and alkali land into a single "urban/bare" class for each of the four land-cover maps.

Second, we overlaid the reclassified images on the $1\ \mathrm{km}^2$ grid cells to compute for each cell the percentage of the six land-cover types within it and stored the results in a new attribute table. When calculating the percentage of a land-cover type within a cell, we divided the sum of the land-cover-type area by the area of the cell.

It has to be decided how to process a pixel that is located on a grid line (or spans multiple grid lines). A previous study had assigned a pixel located on a grid line to the cell that covered the largest part of the pixel [21]. However, this method introduces an error due to the spatial resolution of the Landsat data, which may affect the accuracy of the spatial–temporal analysis of land-cover changes and of the calculation of the correlation coefficients. For example, in the worst case, almost 50% of the pixel area (nearly $1800\ \mathrm{m}^2$ of MSS or $450\ \mathrm{m}^2$ of TM/ETM+) may be incorrectly assigned to neighbouring cells.

To reduce the error caused by the pixel size, we resampled each of the four land-cover maps to a 1-m spatial resolution pixel size. After resampling, the area inaccurately assigned to a

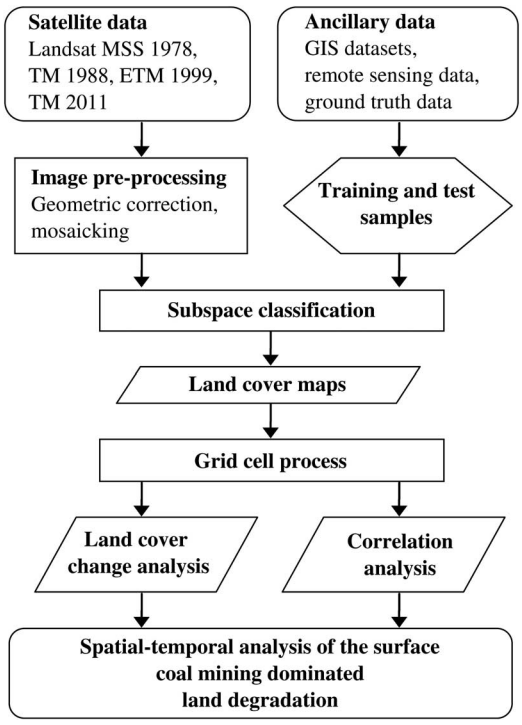

Fig. 3. Flowchart for the procedures performed in the study.

TABLE III
CONFUSION MATRICES OF OBTAINED LAND-COVER MAPS

(a) Confusion matrix for the 1978 land-cover map

1978	1	2	3	4	5	6	7	8	9	Σ	UA (%)
1. Water	***162***	0	4	0	0	0	0	0	0	166	97.59
2. Forest	0	***345***	0	1	0	0	21	0	69	436	79.13
3. Grassland	25	0	***294***	17	1	0	0	0	0	337	87.24
4. Sparse	1	0	39	***146***	17	4	0	9	2	218	66.97
5. Barren	0	0	14	0	***120***	17	0	45	0	196	61.22
6. Sandy	0	0	0	15	30	***202***	0	14	0	261	77.39
7. Wetland	21	96	13	0	0	0	***277***	0	83	490	56.53
8. Cropland	0	0	5	24	27	15	0	***97***	0	168	57.74
9. Dense	0	50	0	0	0	0	4	0	***63***	117	53.85
Σ	209	491	369	203	195	238	302	165	217	2389	
PA (%)	77.51	70.26	79.67	71.92	61.54	84.87	91.72	58.79	29.03		
OA (%)	71.4										
Kappa	0.6729										

(b) Confusion matrix for the 1988 land-cover map

1988	1	2	3	4	5	6	7	8	9	10	11	Σ	UA (%)
1. Water	***548***	1	19	1	0	0	38	55	6	0	0	668	82.04
2. Forest	2	***1154***	1	0	0	0	9	0	0	0	111	1277	90.37
3. Grassland	48	0	***1193***	113	4	0	4	38	3	3	43	1449	82.33
4. Sparse	21	0	108	***708***	27	26	0	20	21	0	0	931	76.05
5. Urban	1	0	0	17	***157***	0	0	20	52	0	0	247	63.56
6. Sandy	0	0	0	16	0	***654***	0	3	54	0	0	727	89.96
7. Wetland	36	51	3	0	0	0	***471***	0	0	0	9	570	82.63
8. Cropland	0	0	6	3	0	0	0	***369***	3	4	0	385	95.84
9. Barren	0	0	0	19	40	47	0	11	***356***	0	0	473	75.26
10. Coal	0	0	0	0	0	0	0	0	0	***84***	0	84	100
11. Dense	30	137	151	5	0	0	154	0	0	0	***480***	957	50.16
Σ	686	1343	1481	882	228	727	676	516	495	91	643	7768	
PA (%)	79.88	85.93	80.55	80.27	68.86	89.96	69.67	71.51	71.92	92.31	74.65		
OA (%)	80.5												
Kappa	0.7693												

(c) Confusion matrix for the 1999 land-cover map

1999	1	2	3	4	5	6	7	8	9	10	11	12	Σ	UA (%)
1. Water	***976***	0	0	1	13	0	6	36	2	0	1	0	1035	94.3
2. Forest	0	***579***	16	0	0	0	41	16	0	0	1	0	653	88.67
3. Grassland	0	40	***1251***	34	3	0	52	35	0	2	11	32	1460	85.68
4. Sparse	0	1	36	***268***	0	7	0	34	5	0	1	2	354	75.71
5. Urban	12	0	0	0	***237***	0	0	0	9	7	0	0	265	89.43
6. Sandy	0	0	0	24	0	***407***	0	4	29	0	1	1	466	87.34
7. Wetland	46	46	90	0	0	0	***379***	43	0	0	25	0	629	60.25
8. Cropland	1	8	32	15	7	0	0	***333***	0	3	50	1	442	75.34
9. Barren	10	0	0	0	1	28	0	0	***910***	2	0	41	992	91.73
10. Coal	0	0	0	0	0	0	0	58	2	***322***	0	0	382	84.29
11. Dense	0	34	50	0	0	0	11	26	0	0	***548***	0	669	81.91
12. Alkali soils	7	0	4	3	23	1	0	16	17	0	0	***434***	505	85.94
Σ	1052	700	1479	345	284	443	489	601	974	336	638	511	7852	
PA (%)	92.78	82.71	84.58	77.68	83.45	91.87	77.51	55.41	93.43	95.83	85.89	84.93		
OA (%)	84.6													
Kappa	0.8280													

(d) Confusion matrix for the 2011 land-cover map

2011	1	2	3	4	5	6	7	8	9	10	11	12	Σ	UA (%)
1. Water	***691***	1	28	0	6	0	22	27	0	0	0	0	775	89.16
2. Forest	1	***1095***	1	0	0	0	64	36	0	0	13	0	1210	90.5
3. Grassland	5	17	***1249***	37	84	0	43	15	0	0	151	2	1603	77.92
4. Sparse	1	0	0	***468***	19	20	0	6	43	0	17	77	651	71.89
5. Urban	20	0	10	3	***420***	0	0	0	40	12	0	69	574	73.17
6. Sandy	0	0	0	56	0	***972***	0	8	47	0	0	7	1090	89.17
7. Wetland	7	119	1	0	0	0	***542***	0	0	0	38	0	707	76.66
8. Cropland	1	2	11	34	19	1	1	***454***	51	11	11	9	605	75.04
9. Barren	1	0	0	5	54	29	0	0	***752***	14	0	35	890	84.49
10. Coal	6	0	0	0	0	0	0	0	1	***697***	0	0	704	99.01
11. Dense	4	141	26	1	2	0	61	74	0	0	***490***	0	799	61.33
12. Alkali soils	2	0	4	24	50	0	0	1	103	0	0	***536***	720	74.44
Σ	739	1375	1330	628	654	1022	733	621	1037	734	720	735	10328	
PA (%)	93.5	79.64	93.91	74.52	64.22	95.11	73.94	73.11	72.52	94.96	68.06	72.93		
OA (%)	81													
Kappa	0.7910													

UA, user's accuracy; PA, producer's accuracy; OA, overall accuracy; Kappa, kappa coefficient.

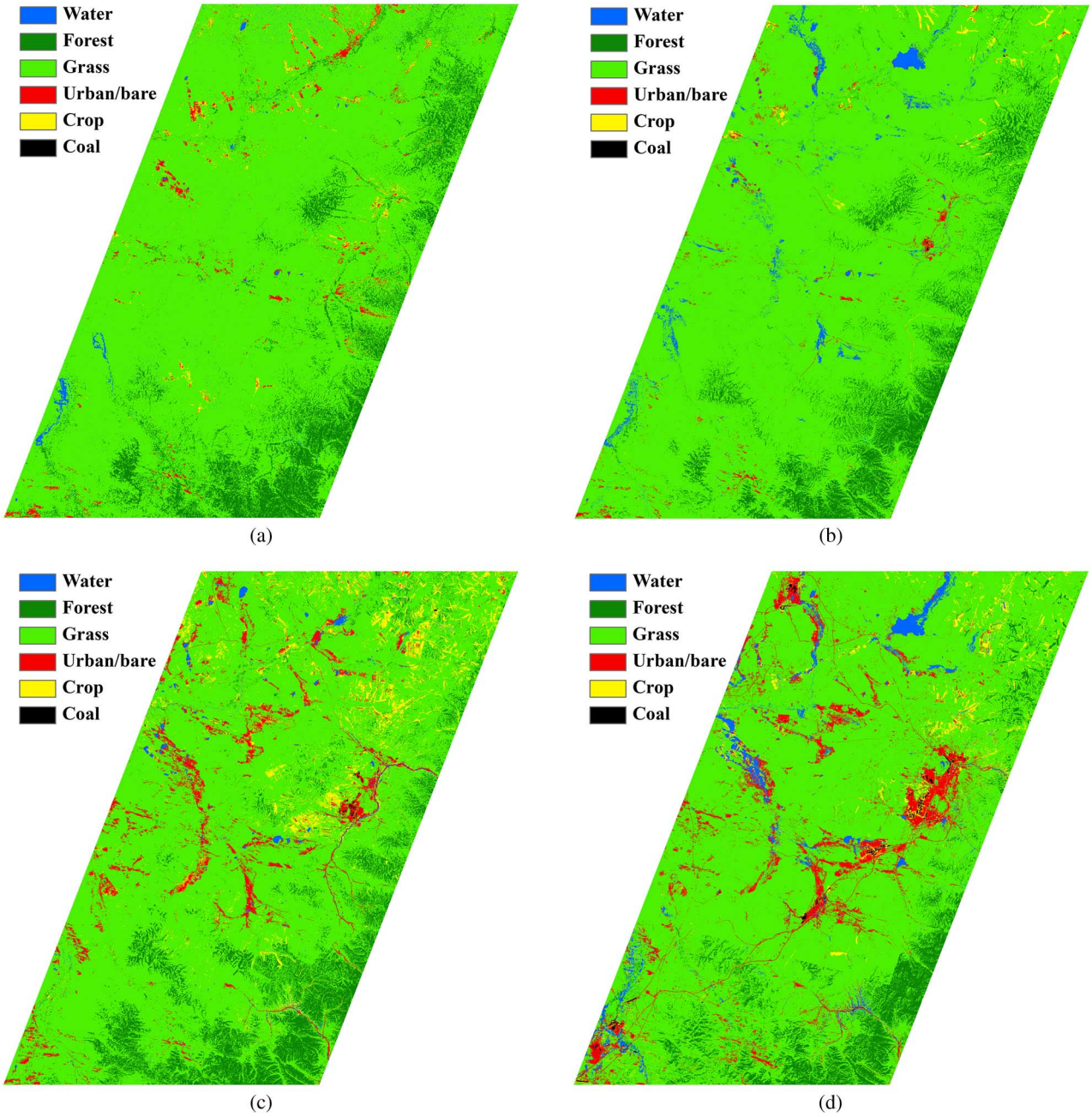

Fig. 4. Time series of land-use and land-cover maps of the study area in: (a) 1978, (b) 1988, (c) 1999, and (d) 2011.

neighbouring cell's pixel area became less than $0.5\ \mathrm{m}^2$. We then assigned such a pixel located on a grid line (or spanning multiple grid lines) to the cell that covered the largest part of the pixel.

Finally, the land-cover maps were expressed as a percentage of each of the six land-cover types for each of the grid cells. Thus, the grid cells enable us to aggregate the categories for each map and to calculate their proportions in $1\ \mathrm{km}^2$ grid cells. Furthermore, they enable us to evaluate the spatial–temporal changes in land-cover categories to allow a much easier statistical comparison of the land-cover changes.

Fig. 3 depicts the flowchart that explains how the research data, methods, and analysis were organized in a brief way.

IV. Results

A. Spatial–Temporal Changes of the Land-Cover Classes

The subspace method classification was performed for each of four mosaicked Landsat images with accuracies ranging between 71.4% and 84.6% for the test dataset (Table III). In this study, the subspace dimensions were fixed as two for the 1978 MSS, and three for the 1988 TM image, 1999 ETM+, and 2011 TM images.

Class-specific accuracies were satisfactory for landscape-scale monitoring; in particular, the producer's and user's accuracies for the most important coal class were better than 90% and 80%, respectively. Grassland showed a high accuracy ranging from

77.92% to 93.91%. However, as shown in Table III, the barren class was the most difficult of all categories to classify and was confused mainly with sandy land and cropland for 1978 MSS, sandy land and urban for 1988 TM, sandy land for 1999 ETM+, and alkali soils for 2011 TM datasets.

The low producer's accuracy (68.86% in 1988 and 64.22% in 2011) and low user's accuracy (63.56% in 1988 and 73.17% in 2011) of the urban class were possibly due to the fact that the roofs of the houses in rural villages were usually soil-covered in 1978 and were made of adobe blocks after 1988. Thus, house areas tended to be mislabelled as barren class.

The relatively low producer's accuracies of the cropland class (58.79% in 1978 and 55.41% in 1999) were because cropland pixels could not be separated well from barren class pixels so they were mislabelled as barren for the 1978 map. In the 1999 map, significant numbers of cropland pixels were misclassified to water, grassland, sparse, and coal classes because of the existence of aquatic plants and crop cultivation combined with pasture growing, as well as the difficulty in distinguishing whether cropland had been abandoned. In the 1978 and 2011 maps, the producer's accuracy for the dense grass class was as low as 29.03% and 68.06%, respectively, because dense grass was mislabelled as wetland or grassland.

As described in Section III, after aggregation, the final six categories in the land-cover maps were water, forest, grassland, urban/bare, cropland, and coal. After-aggregation land-cover classification maps for each of the 4 years are shown in Fig. 4, and detailed land-cover maps for the area around the Holingol open pit coal mine are shown in Fig. 5 (see Fig. 1 for the location of the detailed maps).

As can be seen in Figs. 4 and 5, there was a remarkable increase in urban/bare and coal-mining areas, and a decrease in grassland area. While the area of cropland increased from 1978 to 1999, the cropland area tended to decrease from 1999.

The area of coal stockpiles in 2011 was more than 14 times the area in 1988, an increase from 0.02% in 1988 to 0.29% in 2011. The area of urban/bare has more than quadrupled over the past three decades, increasing from 1.61% of the study area in 1978 to 7.18% in 2011. The area of grassland decreased from 86% in 1978 to 78.8% in 1999. However, after 1999, the area of grassland increased to 80.5% by 2011.

Cropland at first rapidly increased from 1.07% in 1978 to 5.01% in 1999 and then decreased to 2.49% in 2011. In fact, a policy of returning farmland to forest and grassland has been put into practice, since 2000. As a result, in Huolinguole, cropland decreased from 17 134 ha in 1998 [27] to 12 697 ha in 2010 [7].

Fig. 6(a) shows the grid-cell-based spatial change of urban/bare area from 1978 to 2011. The value of each grid square cell was calculated by subtracting the urban/bare area of 1978 from that of 2011 in each grid cell and then dividing the changed area by the cell area. As Fig. 6(a) illustrates, the urban/bare area rapidly expanded around the three main coal fields (Fig. 1).

Fig. 6(b) shows the grid-cell-based spatial change of coal-mining area from 1978 to 2011, which was calculated in the same way as for Fig. 6(a). Typically, the coal-mining area increased rapidly in the three coal fields.

Fig. 6(c) shows the grid-cell-based spatial change of grassland area from 1978 to 2011, which was calculated in the same way as for Fig. 6(a). The grassland area decreased rapidly around the three coal fields, but in some regions the grassland tended to increase. The grassland increase trends were the result of two government initiatives: the Sandstorm Source Control project and the Ecological Migration project. These government policies led to an increase in grassland.

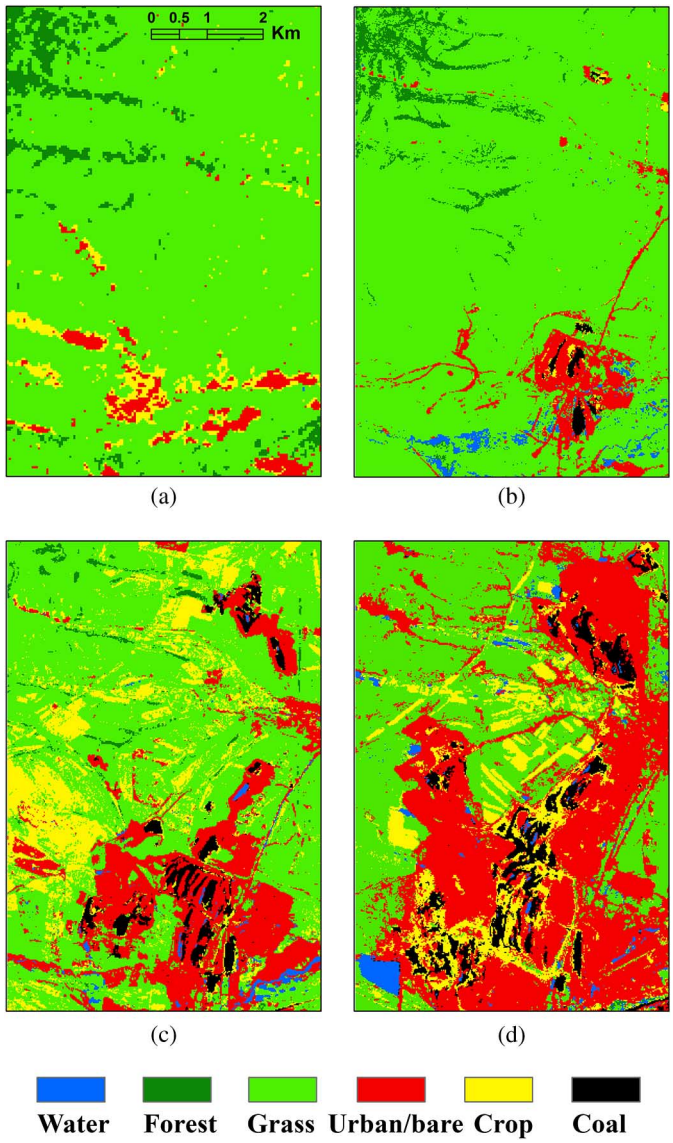

Fig. 5. Time series of detailed land-cover maps around Holingol open pit coal mine in the study area for: (a) 1978, (b) 1988, (c) 1999, and (d) 2011. The location of maps is shown in Fig. 1.

B. Relationship Among the Land-Cover Changes

To investigate the relationship among the land-cover changes caused by coal-mine expansion, we calculated the correlation coefficients (r) of the land-cover categories (i.e., water, forest, grassland, urban/bare, cropland, and coal) based on the $1\ \mathrm{km}^2$ grid square cells. Table IV presents a summary of the linear correlation coefficient matrix among the changes of land-cover categories from 1978 to 2011 based on 10 383 grid cells (samples).

As shown in Table IV, the linear correlation coefficient was -0.29 between coal and grassland classes, -0.67 between

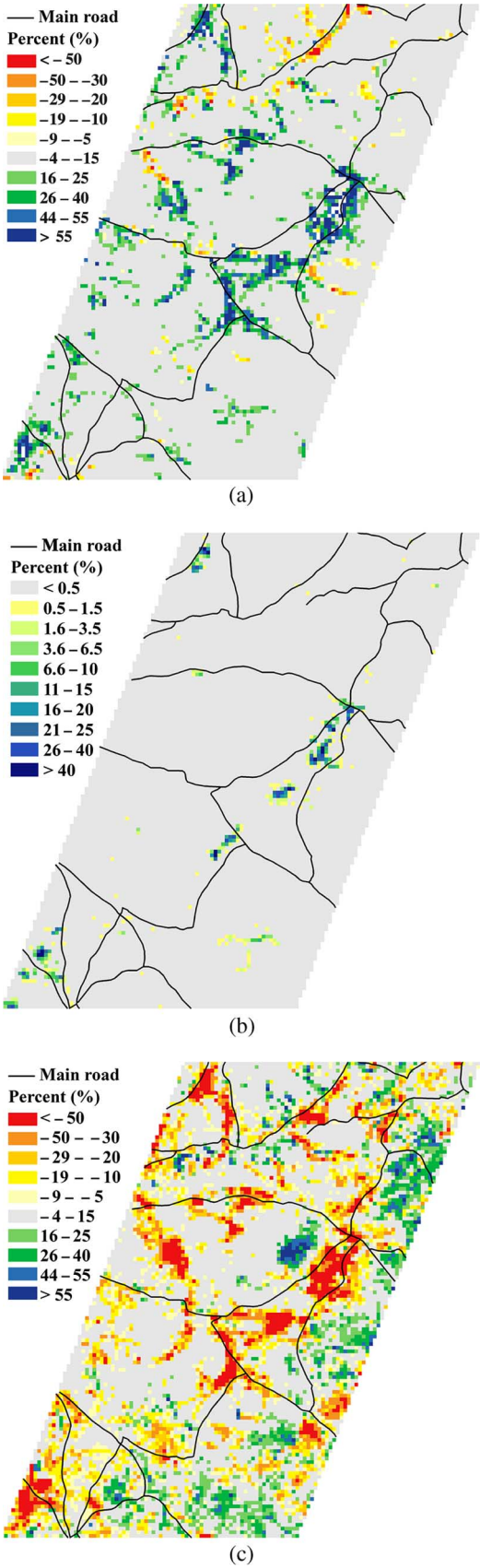

Fig. 6. Spatial–temporal analysis from 1978 to 2011: (a) urban/bare, (b) coal stockpiles, and (c) grassland.

TABLE IV
CORRELATIONS AMONG LAND-COVER CATEGORIES DURING 1978–2011

r	Water	Forest	Grassland	Urban/bare	Cropland	Coal
Water	1					
Forest	–0.0281	1				
Grassland	–0.3898	–0.5269	1			
Urban/bare	0.0042	0.0159	–0.6722	1		
Cropland	0.0072	–0.0725	–0.3345	0.0711	1	
Coal	0.0286	0.0003	–0.2923	0.2078	0.1443	1

urban/bare and grassland classes, 0.21 between coal and urban/bare, -0.39 between grassland and water, and -0.33 between grassland and cropland classes. The correlations between coal, urban/bare, and grassland change were statistically significant.

In fact, in open-cast mining, the surface earth and underground soil are peeled off and piled on the earth's surface, turning it into bare soil. This generally causes a decline in herbaceous ground cover and marked increases in barren area [28]. In addition, many mountains covered with grass were stripped to provide materials (soil and rock) for the construction of the necessary roads and urban and coal industrial parks. Meanwhile, grassland correlated negatively with cropland ($r = -0.33$) owing to human population growth, which was mainly migration attracted by the coal industry, and more and more cropland was needed to feed them. As shown in Fig. 4, during 1978–1998, a vast area of grassland area was turned into cropland. Since 1999, this tendency has weakened owing to the policy of the Sandstorm Source Control project and the Ecological Migration project [29].

Fig. 7(a) shows the strong negative relationship between urban/bare and grassland changes during 1978–2011. Fig. 7(b) represents the positive relationship between coal and urban/bare changes, which indicates that the rapid urbanization of Holingol is driven by the expansion of a coal energy-based industry, as no other industry is available [27]. Fig. 7(c) shows the negative relationship between coal and grassland changes. Fig. 7(d) shows the how grassland and cropland are negatively correlated.

To better understand the trends of grassland changes, coal mine expansion, urbanization, and other ecosystem dynamics, we divided the land-cover changes during 1978–2011 into three time intervals: 1978–1988, 1988–1999, and 1999–2011. Results from our correlation analyses show that grassland was continually and negatively correlated with urban/bare (-0.37, -0.46, and -0.14, respectively) and cropland (-0.43, -0.09, and -0.15, respectively). The correlation between grassland and coal classes was very weak in 1978–1988 (-0.09) and in 1988–1999 (0.07). However, the correlation coefficient of coal versus grassland turned negative (-0.21) in 1999–2011. This change was due to the rapid expansion of coal-mining activities that converted grassland into other land-cover types.

V. DISCUSSION

There were no mining activities at the study area in 1978, except for the Holingol open pit coal mine, which was mostly undergoing preparatory work for the coal-mining project. However, a large-scale surface coal-mining boom started during the

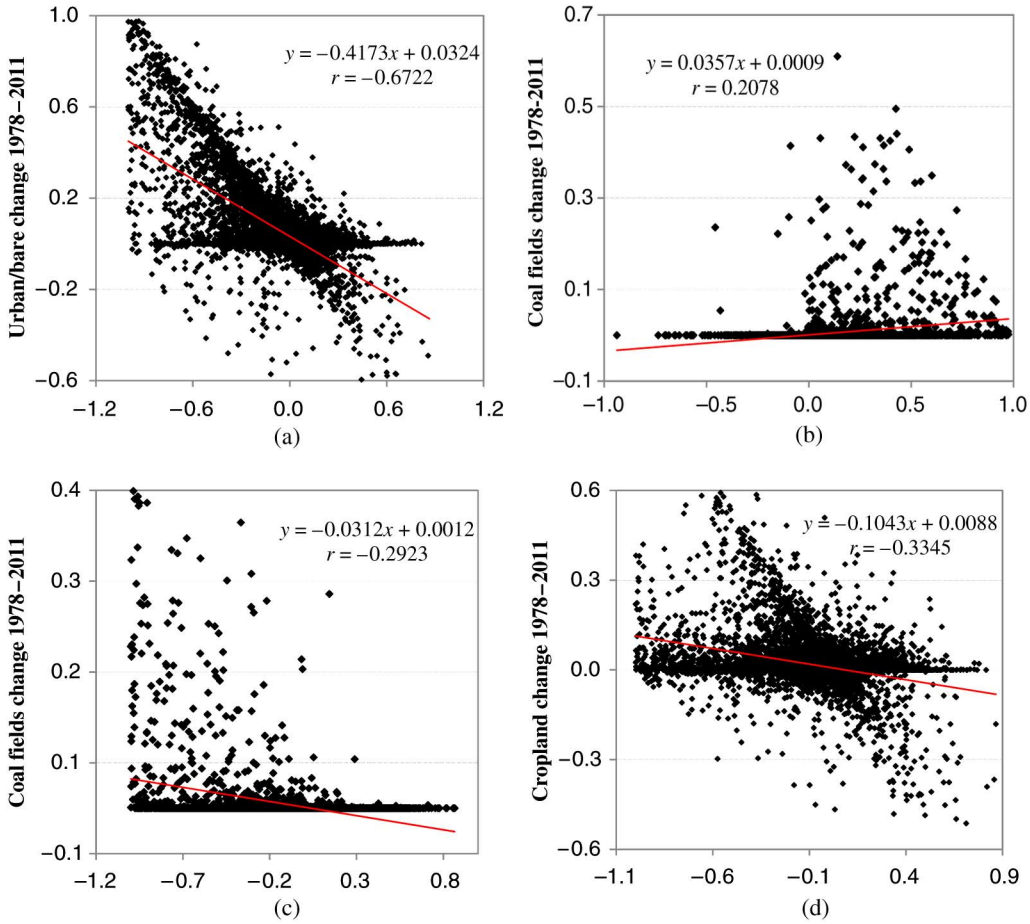

Fig. 7. Representative scatter plots of land-cover categories for 1978–2011. The total points are 10 383 samples (grid cells): (a) grassland change 1978–2011, (b) urban/bare change 1978–2011, (c) grassland change 1978–2011, and (d) grassland change 1978–2011.

TABLE V
YEARLY PRODUCTION CAPACITY OF COAL MINES IN HOLINGOL, FROM 1976 TO 2004

Year	Production capacity of coal mines (tons per year)
1976–1978	Preparation phase for mining
1979–1984	300 000
1984–1992	10 000 000
1992–1999	10 000 000
1999–2004	12 500 000

1980s. Table V shows the production capacity of exploiting coal resources at Holingol coal mines from 1976 to 2004. As shown in Table V, this period of expansion resulted in a quadrupling of coal production capacity.

Coal mining is a major contributor to ecological and environmental degradation [30]. Coal mining drastically destroys grassland and generates waste materials from open-cast coal occupying vast areas of grassland, which causes long-term damage to the grassland ecosystem.

Meanwhile, heavy industries related to coal mines, such as coal mining, coal-based power generation, and petrochemical processing, are created with the sacrifice of a huge amount of water resources. To meet the water demands of coal-based industries, local rivers and their tributaries were dammed and numerous wells were digged. This results in the drying up of lakes, streams, and critical wetlands.

In addition, a government-planned migration of farmers to cultivate the natural pasture of the Wulagai River region of East Ujimqin Banner began around 1985. Moreover, accompanying the coal-mining boom, many farmers also migrated into the Holingol region, while grasslands reclamation was being introduced largely to the west and north of the region. After 1999, cropland cultivation stopped and tended to decrease owing to the government initiative of returning cropland to grassland and forest [31]. Our results confirm that the policy shift suppressed cropland area in the Holingol region.

Other contributors to grassland degradation include rapidly increased population growth, urbanization, and infrastructure development, including planned roads and railroads. For example, because of the rapid growth of coal mining, the overall population of Huolinguole increased from 29 897 in 1985 to 82 430 in 2010, which caused large areas of grassland to be transformed into coal-related industries and urban built-up area. Roads and railroads built to transport coal not only cause grassland degradation, but may be the greatest threat to biodiversity because roads and railroads can effectively divide formerly contiguous populations of terrestrial wildlife.

It should also be noted that for the subspace method, the overlap between low-dimensional class subspaces is reduced enough in the high-dimensional space, and thus the performance using the subspace method on 1988 TM, 1999 ETM+, and 2011 TM gives higher overall classification accuracies (Table III). However, on the 1978 MSS, the subspace method gives the lowest overall classification accuracy (Table III). The reason for this is mainly due to the overlap between class subspaces in low-dimensional data space. As the subspace method can be directly implemented on a high-dimensional dataset without band optimization processing, it is possible to map the data space into a higher dimensional feature space by kernel-based methods in order to reduce the overlap between subspaces, while maintaining computational simplicity of the subspace learning procedure.

VI. Conclusion

Grassland degradation and urbanization in the Holingol region from 1978 to 2011 have been identified, quantified, and analysed by using multi-temporal Landsat data. The expansion of mining activities, coal-related industries, and population increases was the major contribution to the conversion of grassland to other land-use types. A grid-square-based spatial correlation analysis showed that mining area expansion was strongly positively correlated with urban area expansion and strongly negatively correlated with grassland change. Furthermore, a spatial correlation analysis of three time intervals (i.e., 1978–1988, 1988–1999, and 1999–2011) allowed us to describe the spatial–temporal dynamics of the mine and urban growth patterns in more detail.

The coal-mining boom and mine development are major concerns for biodiversity over the next decade. Further study should explore the land degradation and decline in biodiversity caused by road construction.

References

[1] S. Brogaard and X. Y. Zhao, "Rural reforms and changes in land management and attitudes: A case study from Inner Mongolia, China," *Ambio A J. Human Environ.*, vol. 31, no. 3, pp. 219–225, May 2002.

[2] Wulantuya, "Land reclamation and land-use changes during last 50 years in Ke'erqin deserts, Inner Mongolia," *Progr. Geogr.*, vol. 19, no. 3, pp. 273–278, 2000 (in Chinese with English abstract).

[3] H. Bagan, W. Takeuchi, T. Kinoshita, Y. Bao, and Y. Yamagata, "Land cover classification and change analysis in the Horqin Sandy Land from 1975 to 2007," *IEEE J. Sel. Topics Appl. Earth Observ.*, vol. 3, no. 2, pp. 168–177, Jun. 2010.

[4] Y. Chen, A. Ebenstein, M. Greenstone, and H. Li, "Evidence on the impact of sustained exposure to air pollution on life expectancy from China's Huai River policy," *Proc. Nat. Acad. Sci.*, vol. 110, no. 32, pp. 12936–12941, 2013.

[5] N. Demirel, M. K. Emil, and H. S. Duzgun, "Surface coal mine area monitoring using multi-temporal high-resolution satellite imagery," *Int. J. Coal Geol.*, vol. 86, no. 1, pp. 3–11, Apr. 2011.

[6] Subuda, J. Yi, J. Chen, X. Bao, and Sanasiqin, "Analysis of vegetation degeneration succession trend in middle and lower reaches of Wulagai wetland of Inner Mongolia," *Chin. J. Grassland*, vol. 33, no. 3, pp. 73–78, 2011 (in Chinese with English abstract).

[7] Survey office of Statistical Bureau of Huolinguole, *Huolinguole Statistical Yearbook of 2010.* Holinguole, Inner Mongolia, China: Huolinguole Statistical Bureau, 2011, ch, 2, sec. 3, p. 91.

[8] C. Zan, Y. Bai, and P. Lei, "The investigation of land reclamation situation of Wulagai Comprehensive Economy Developed Area," *North. Environ.*, vol. 22, no. 1, pp. 40–42, Jan. 2010 (in Chinese with English abstract).

[9] H. Jiang, "Grassland management and views of nature in China since 1949: Regional policies and local changes in Uxin Ju, Inner Mongolia," *Geoforum*, vol. 36, no. 5, pp. 641–653, Sep. 2005.

[10] C. Potter, V. Genovese, P. Gross, S. Boriah, M. Steinbach, and V. Kumar, "Revealing land cover change in California with satellite data," *Eos Trans. Am. Geophys. Union*, vol. 88, no. 26, p. 269, Jun. 2007.

[11] A. Fernández-Manso, C. Quintano, and D. Roberts, "Evaluation of potential of multiple endmember spectral mixture analysis (MESMA) for surface coal mining affected area mapping in different world forest ecosystems," *Remote Sens. Environ.*, vol. 127, pp. 181–193, Dec. 2012.

[12] L. J. M. Jansen, M. Bagnoli, and M. Focacci, "Analysis of land-cover/use change dynamics in Manica Province in Mozambique in a period of transition (1990–2004)," *Forest. Ecol. Manage.*, vol. 254, no. 2, pp. 308–326, Jan. 2008.

[13] D. Lu, P. Mausel, E. Brondizio, and E. Moran, "Change detection techniques," *Int. J. Remote Sens.*, vol. 25, no. 12, pp. 2365–2407, Jun. 2004.

[14] K. M. Bergen, T. Zhao, V. Kharuk, Y. Blam, D. G. Brown, L. K. Peterson, and N. Miller, "Changing regimes: Forested land cover dynamics in central Siberia 1974 to 2001," *Photogramm. Eng. Remote Sens.*, vol. 74, no. 6, pp. 787–798, Jun. 2008.

[15] G. Chander, B. L. Markham, and D. L. Helder, "Summary of current radiometric calibration coefficients for Landsat MSS, TM, ETM+, and EO-1 ALI sensors," *Remote Sens. Environ.*, vol. 113, no. 5, pp. 893–903, May 2009.

[16] B. Waske and S. Van der Linden, "Classifying multilevel imagery from SAR and optical sensors by decision fusion," *IEEE Trans. Geosci. Remote Sens.*, vol. 46, no. 5, pp. 1457–1466, May 2008.

[17] P. Griffiths, P. Hostert, O. Gruebner, and S. Van Der Linden, "Mapping megacity growth with multi-sensor data," *Remote Sens. Environ.*, vol. 114, no. 2, pp. 426–439, Feb. 2010.

[18] E. Oja, *Subspace Methods of Pattern Recognition.* Letchworth, U.K.: Research Studies Press and Wiley, 1983.

[19] H. Bagan and Y. Yamagata, "Improved subspace classification method for multispectral remote sensing image classification," *Photogramm. Eng. Remote Sens.*, vol. 76, no. 11, pp. 1239–1251, Nov. 2010.

[20] C. Small, C. D. Elvidge, D. Balk, and M. Montgomery, "Spatial scaling of stable night light," *Remote Sens. Environ.*, vol. 115, pp. 269–280, 2011.

[21] H. Bagan and Y. Yamagata, "Landsat analysis of urban growth: How Tokyo became the world's largest megacity during the last 40 years," *Remote Sens. Environ.*, vol. 127, pp. 210–222, Dec. 2012.

[22] C. G. Homer, R. D. Ramsey, C. T. Edwards, Jr., and A. Falconer, "Landscape cover-type modelling using a multi-scene Thematic Mapper mosaic," *Photogramm. Eng. Remote Sens.*, vol. 63, no. 1, pp. 671–677, Jan. 1997.

[23] J. Liu, M. Liu, H. Tian, D. Zhuang, Z. Zhang, W. Zhang, X. Tang, and X. Deng, "Spatial and temporal patterns of China's cropland during 1990–2000: An analysis based on Landsat TM data," *Remote Sens. Environ.*, vol. 98, no. 4, pp. 442–456, Oct. 2005.

[24] LREIS Data, *Resources and Environment Database of China (1:4,000,000).* Beijing, China: State Key Laboratory of Resources and Environment Information System, Institute of Geographic Sciences and Natural Resources Research, Chinese Academy of Sciences, 1996 (with CD-ROM).

[25] R. G. Congalton and K. Green, *Assessing the Accuracy of Remotely Sensed Data: Principles and Practices.* Boca Raton, FL, USA: Lewis, 1999.

[26] H. Bagan, Y. Yasuoka, T. Endo, X. Wang, and Z. Feng, "Classification of airborne hyperspectral data based on the average learning subspace method," *IEEE Geosci. Remote Sens. Lett.*, vol. 5, no. 3, pp. 368–372, Jul. 2008.

[27] Local Chronicles Compiling Committee of Holinguole City, *Local Chronicles of Holinguole City from 1994–2006.* Hulunbuir, Inner Mongolia, China: Inner Mongolia Cultural Press, 2008, pp, 156–271.

[28] National Research Council, *Coal Research and Development to Support National Energy Policy.* Washington, DC, USA: National Academies Press, 2007.

[29] G. Zhang, J. Dong, X. Xiao, Z. Hu, and S. Sheldon, "Effectiveness of ecological restoration projects in Horqin Sandy Land, China based on SPOT-VGT NDVI data," *Ecol. Eng.*, vol. 38, no. 1, pp. 20–29, Jan. 2012.

[30] J. Dowarah, H. P. Deka Boruah, J. Gogoi, N. Pathak, N. Saikia, and A. K. Handique, "Eco-restoration of a high-sulphur coal mine overburden dumping site in northeast India: A case study," *J. Earth Syst. Sci.*, vol. 118, no. 5, pp. 597–608, Oct. 2009.

[31] J. Dong, J. Liu, H. Yan, F. Tao, and W. Kuang, "Spatio-temporal pattern and rationality of land reclamation and cropland abandonment in mid-eastern Inner Mongolia of China in 1990–2005," *Environ. Monit. Assess.*, vol. 179, no. 1–4, pp. 137–153, Aug. 2011.

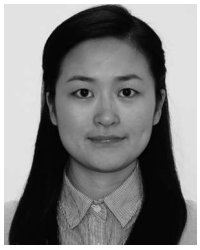

Tana Qian received the B.S. degree in School of Economic Administration, Dalian Nationalities University, Dalian, China, in 2010. She is working toward the M.S. degree at the School of Agriculture, Ibaraki University, Amimachi, Japan, with an emphasis in remote sensing.

Currently, she is a Research Assistant with the National Institute for Environmental Studies, Tsukuba, Japan.

Hasi Bagan (M'07) received the B.S. degree in mathematics from the Peking University, Beijing, China, in 1991, the M.S. degree in mathematics from the Beijing University of Aeronautics and Astronautics, Beijing, China, in 1996, and the Ph.D. degree from the Institute of remote sensing applications, Chinese Academy of Sciences, Beijing, China, in 2004.

From 2004 to 2006, he was a Postdoctoral Researcher with the National Institute for Environmental Studies, Tsukuba, Japan. From 2006 to 2008, he was a JSPS Postdoctoral Fellow with the Institute of Industrial Science, The University of Tokyo, Tokyo, Japan. Currently, he is a Research Associate with the National Institute for Environmental Studies, Japan. His research interests are land-cover classification, neural network, wavelet fusion, and subspace algorithms.

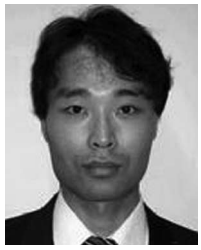

Tsuguki Kinoshita received the B.Eng., the M.Eng. degrees in naval architecture, and the Doctor of Engineering degree from The University of Tokyo, Tokyo, Japan, in 1993, 1996, and 1999, respectively.

Currently, he is an Associate Professor with the College of Agriculture, Ibaraki University, Amimachi, Japan. His research topic is global land-use modeling and woody biomass potential survey.

Mr. Kinoshita is also a member of Representative Concentration Pathways (RCPs) task team.

Yoshiki Yamagata received the Ph.D. degree in system science from the University of Tokyo, Tokyo, Japan, in 1998.

Since 1991, he works at the National Institute for Environmental Studies (NIES), Tsukuba, Japan. Currently, he is studying about the climate risk management as a Principal Researcher at the Center for Global Environmental Research (CGER), Tsukuba, Japan. He is also affiliated with IIASA, Vienna, Austria, and Institute of Statistical Mathematics (ISM) Tokyo, Japan. His recent research topics include land use scenarios, resilient urban planning, and spatial network analysis.

He has lecture series at the University of Tokyo, University of Tsukuba, Tsukuba, Japan, and Hokkaido University, Sapporo, Japan. Internationally, he has contributed as Lead Author of IPCC, Steering Committee of "Global Carbon Project," and Editor of "Applied Energy."